

**OPEN ACCESS**

# Na-Ion Desalination (NID) Enabled by Na-Blocking Membranes and Symmetric Na-Intercalation: Porous-Electrode Modeling

To cite this article: Kyle C. Smith and Rylan Dmello 2016 *J. Electrochem. Soc.* **163** A530

View the [article online](#) for updates and enhancements.

## You may also like

- [Network structure exploration via Bayesian nonparametric models](#)  
Y Chen, X L Wang, X Xiang et al.
- [Comment on: "Na-Ion Desalination \(NID\) Enabled by Na-Blocking Membranes and Symmetric Na-Intercalation: Porous-Electrode Modeling" \[\*J. Electrochem. Soc.\*, 163, A530 \(2016\)\]](#)  
Kyle C. Smith and Rylan Dmello
- [Correlative investigation of Mg doping in GaN layers grown at different temperatures by atom probe tomography and off-axis electron holography](#)  
Lynda Amichi, Isabelle Mouton, Victor Bureau et al.



## Your Lab in a Box!

The PAT-Tester-i-16: All you need for Battery Material Testing.

- ✓ All-in-One Solution with integrated Temperature Chamber!
- ✓ Cableless Connection for Battery Test Cells!
- ✓ Fully featured Multichannel Potentiostat / Galvanostat / EIS!

[www.el-cell.com](http://www.el-cell.com) +49 40 79012-734 [sales@el-cell.com](mailto:sales@el-cell.com)

**EL-CELL**<sup>®</sup>  
electrochemical test equipment





# Na-Ion Desalination (NID) Enabled by Na-Blocking Membranes and Symmetric Na-Intercalation: Porous-Electrode Modeling

Kyle C. Smith<sup>\*,z</sup> and Rylan Dmello

Department of Mechanical Science and Engineering and Computational Science and Engineering Program, University of Illinois at Urbana-Champaign, Urbana, Illinois 61801, USA

A new device concept, Na-Ion Desalination (NID), is introduced to desalinate NaCl from water using Na-ion battery (NIB) intercalants. A two-dimensional porous-electrode model is used to predict the performance of NID cells operating at sea- and brackish-water salinity-levels by simulating electrolyte transport, membrane polarization, and simultaneous electrochemistry. Anion-selective membranes are used to isolate electrodes in NID cells because simulations showed substantial drop from influent salinity (63%) compared to porous separators used in conventional NIBs (22%). Symmetric NIB intercalants and energy recovery were used to minimize energy consumption. A  $\text{Na}_{0.44}\text{MnO}_2$ -based NID-cell with 0.5 mm-thick electrodes desalinated 700 mM influent by 63% while consuming only 50% more energy ( $0.74 \text{ kWh/m}^3$ ) than thermodynamic minimum when cycled at C/2 rate. The high volumetric charge-capacity of NIB intercalants enabled 59–64% drop in influent salinity with water-recovery levels up to 80% and 95% for 700 mM and 70 mM influent, respectively. The present predictions of NID performance are optimistic (side reactions, intercalant decomposition, membrane leakage, and competing cation-intercalation are neglected), providing mechanistic insights into NID operation that will guide NID development in the future.

© The Author(s) 2016. Published by ECS. This is an open access article distributed under the terms of the Creative Commons Attribution Non-Commercial No Derivatives 4.0 License (CC BY-NC-ND, <http://creativecommons.org/licenses/by-nc-nd/4.0/>), which permits non-commercial reuse, distribution, and reproduction in any medium, provided the original work is not changed in any way and is properly cited. For permission for commercial reuse, please email: [oa@electrochem.org](mailto:oa@electrochem.org). [DOI: 10.1149/2.0761603jes] All rights reserved.

Manuscript submitted June 16, 2015; revised manuscript received November 16, 2015. Published January 5, 2016; publisher error corrected January 21, 2016.

Widespread water scarcity makes cheap, high efficiency desalination systems a global priority.<sup>1</sup> Worldwide installed seawater and brackish water desalination capacity has been increasing at a rate of ~40% per year in the last decade<sup>2</sup> due to population growth, aquifer shrinkage, and industrial utilization. This increase in worldwide installed desalination capacity has been driven by reverse osmosis, multi-stage flash, and multiple-effect distillation technologies.<sup>3,4</sup> Electrochemical desalination systems, which include electro dialysis and capacitive deionization, are also viable technologies that have been limited to usage in high-recovery and brackish-water desalination respectively. Capacitive deionization (CDI) was first developed in the 1960s,<sup>5</sup> and uses porous carbon electrodes to store salt ions in the electric double-layer to efficiently desalinate brackish water.<sup>6</sup> Recent capacitive-deionization systems use membranes,<sup>7,8</sup> flow-through electrodes,<sup>9</sup> and hybrid CDI<sup>10</sup> systems to improve desalination performance. Electro dialysis systems, used since the 1960s<sup>11</sup> as a competitor to early reverse osmosis technologies, have improved cycling efficiency using electro dialysis reversal (EDR),<sup>12</sup> and charge isolation using porous separators instead of membranes for shielding.<sup>13–15</sup>

Recently, devices that induce localized electric fields have been used to desalinate water, including the ion-concentration polarization<sup>16</sup> (ICP) and electrochemically mediated desalination<sup>17</sup> (EMD) methods. Similarly, the electric field inside Li-ion batteries can induce the simultaneous depletion of salt in one electrode and accumulation in the opposing electrode when cycled at high rate. This “salt depletion effect” can limit cycling capacity of Li-ion batteries,<sup>18</sup> and consequently energy-storage devices are engineered to prevent it from occurring. For the present Na-Ion Desalination (NID) cell, we exploit this effect by blocking Na transport between opposing electrodes to maximize the degree of salt depletion.

Na-ion intercalation materials have historically been researched for energy storage.<sup>19</sup> Recent successful demonstrations of Na-ion batteries (NIBs) using  $\text{NaTi}_2(\text{PO}_4)_3$  (NTP, Ref. 20),  $\text{Na}_{0.44}\text{MnO}_2$  (NMO, Refs. 21,22),  $\text{Na}_2\text{CuFe}(\text{CN})_6$  (Ref. 23), and  $\text{Na}_{2.55}\text{V}_6\text{O}_{16}$  (Ref. 24) have renewed interest in Na-ion intercalation materials.<sup>25,26</sup> While capacity and energy density are not as high as in Li-ion batteries,<sup>27</sup> recent developments in NIBs suggest that they can be manufactured cheaply and electroactive materials can be synthesized by various

methods.<sup>28–32</sup> Improvements in the capacity and cycle life of NIBs have also been obtained recently.<sup>33,34,23,24</sup> NIB intercalants have been used for desalination in hybrid CDI cells in the past.<sup>10</sup> This work demonstrated the stability of intercalants in seawater and corroborated earlier attempts to use  $\text{Na}_{0.44}\text{MnO}_2$  in a desalination cell.<sup>35</sup> An electrochemical cell that uses Na-ion intercalation in both electrodes (as in the NID cell introduced here) could provide enhanced volumetric desalination capacity over a hybrid CDI cell, because Na-ion intercalants store charge inside electroactive particles while capacitive desalination only stores charge in the Helmholtz double-layer.<sup>6</sup> To our knowledge, previously there has been no device proposed to desalinate water that uses an electrochemical cell with symmetric electrodes containing Na-ion intercalants.

We simulate the local electrochemical processes that occur in NID cells to realistically account for nonlinear and non-uniform polarization and intercalation effects. With this approach we explore a variety of cell configurations, comparing between materials, cell dimensions, and operating parameters to determine the limits of performance for NID cells. We first describe the materials, system, and porous-electrode model used presently. The electrochemical processes that occur during cell cycling are then elucidated by examining the transient distributions of intercalated Na in electroactive particles and of salt in the electrolyte. Subsequently, performance is quantified for a range of applied current density and electrode thickness, after which the influence of influent salt-concentration and water-recovery is explored.

## Methodology

**System definition and materials.**—Figure 1 shows the two-dimensional device simulated presently and its dimensions. The NID device is a symmetric Na-ion cell, meaning that it contains the same type of Na intercalant in both electrodes (rather than dissimilar intercalants used in conventional NIBs). These electrodes are chosen with common thickness  $w$  and length  $L$  (Fig. 1b). The electrodes are porous composites, which enables them to conduct electrons and ions along the  $x$ -direction while saline solution flows through them along the  $y$ -direction (Fig. 1b). The two electrodes can be isolated (Fig. 1a) by either a polymeric separator (commonly used in NIBs) or an anion-selective membrane that blocks Na ions.

Next, we describe the operating concept for the present cell. At the beginning of the charge process electroactive material in the cathode acts as a source of Na, while electroactive material in the anode

\*Electrochemical Society Active Member.

<sup>z</sup>E-mail: [kcsmith@illinois.edu](mailto:kcsmith@illinois.edu)

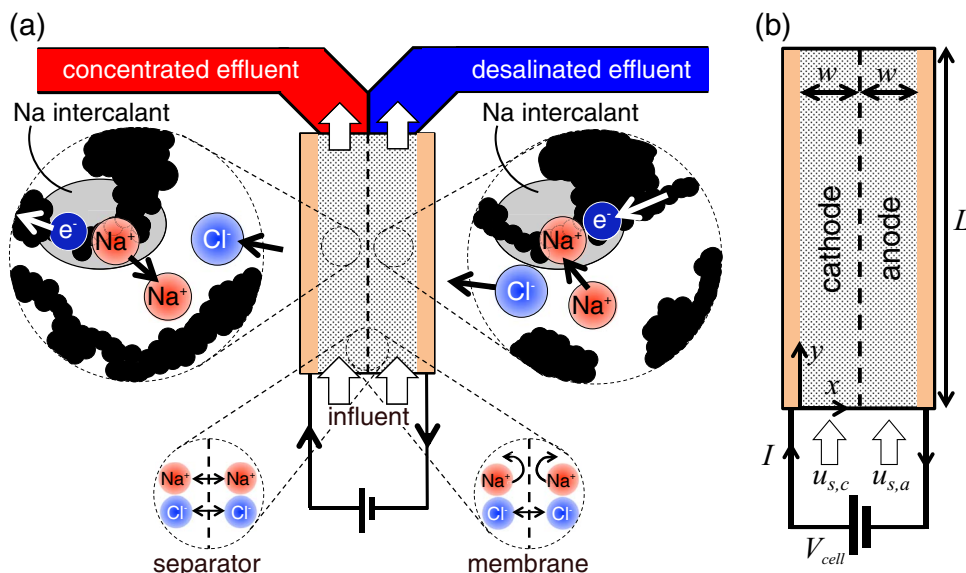


**Figure 1.** Schematic of the desalination device of interest during a charging cycle: (a) Na ions in the cathode (left) de-intercalate from electroactive material into the electrolyte, while Na ions in the anode (right) intercalate into electroactive material. The solution-phase Na-ion concentration-difference between the electrodes drives Cl-ion migration from the anode to the cathode, which in turn concentrates the cathode solution in both Na and Cl ions, while the anode solution is diluted in both. (b) The coordinate system and cell dimensions are shown ( $x$  perpendicular to the current collector and  $y$  along the flow direction).

acts as a sink. Both electrodes contain aqueous NaCl with a certain initial concentration defined by the water source of choice. When charging starts, electrons are released into conductive carbon from the electroactive material in the cathode, which de-intercalates Na ions from the cathode electroactive material into the saline water that flows through the cathode (Fig. 1a, left inset). This electrochemical reaction induces solution-phase charge-imbalance that drives Cl ions from the anode across the separator to the cathode and concentrates cathode solution with Na and Cl ions. A diluted solution forms in the anode (Fig. 1a, right inset) in which electrons enter the anode electroactive material, causing Na ions to intercalate into electroactive material and forcing Cl ions to leave the anode. This process depletes anode solution with Na and Cl ions. Due to the cathode solution being concentrated and the anode solution being diluted simultaneously, effluent streams of two disparate salt concentrations are generated (Fig. 1a, top). The situation is reversed during the discharge cycle, where cathode solution depletes while anode solution concentrates in Na and Cl ions. Since the accumulating and depleting streams are switched during the discharge cycle, the concentrated effluent and desalinated effluent tanks would be switched when the current direction is switched in a practical, experimental device.

The simultaneous accumulation and depletion of electrolyte-phase salt ions in opposing electrodes is known as the salt depletion effect, which was first observed in rocking-chair Li-ion batteries.<sup>18</sup> The proposed desalination method resembles both conventional CDI (due to porous electrodes) and electrodialysis (due to anion-exchange membrane) processes, however it differs from both because it uses Na-ion intercalants to store charge. In addition, the change in cell polarity between the charge and discharge cycles is similar to electrodialysis reversal,<sup>12</sup> which should decrease membrane fouling since there is no buildup of Cl ions at the anion perm-selective membrane.<sup>11</sup> Finally, the anion perm-selective membrane, using the Gibbs-Donnan effect,<sup>36</sup> can sustain a large concentration gradient between the electrodes, allowing significant desalination in the depleted electrode.

**Electrochemical model.**—A porous-electrode model<sup>37</sup> is used here to model Na-ion intercalation, ion transport in flowing NaCl solution, and electron transport inside flow-through electrodes. Overpotential  $\eta$  drives Na-ion intercalation in solid electroactive particles and is defined as  $\eta = \phi_s - \phi_e - \phi_{eq}$ , where  $\phi_s$ ,  $\phi_e$ , and  $\phi_{eq}$  are the solid-phase potential of the electronic conductor, solution-phase potential

of  $\text{Na}^+$ , and the equilibrium potential of Na-ion intercalation, respectively. The solid- and solution-phase potentials are coupled through their respective current-conservation equations (described later). The equilibrium potentials of NTP and NMO vary with the fraction of intercalated Na,  $x_{\text{Na}}$  (defined as the intercalated Na concentration divided by the terminal value). The equilibrium potentials used here, shown in Fig. 2, were estimated from the absolute electrode potentials (i.e., versus a Ag/AgCl reference) measured during charge and discharge of an experimental NMO/NTP cell (Ref. 38) at 0.6 C rate. The terminal concentration of intercalated Na ( $c_{s,max}$ ) by which intercalated-Na fraction is normalized was taken as 14,687 mol-Na/m<sup>3</sup> and 8,095 mol-Na/m<sup>3</sup> for NTP and NMO respectively. These concentrations were chosen to produce theoretical capacities of 133 mAh/g-NTP and 50 mAh/g-NMO reported previously in the literature.<sup>38</sup> The reaction current-density  $i_n$  for intercalation at the surface of electroactive particles is modeled using the Butler-Volmer equation:<sup>39</sup>

$$i_n = i_0 \left[ \exp\left(\frac{0.5F\eta}{R_g T}\right) - \exp\left(-\frac{0.5F\eta}{R_g T}\right) \right], \quad [1]$$

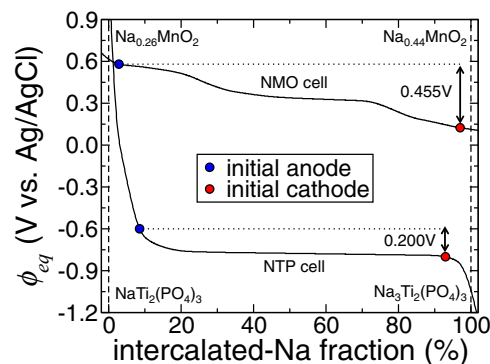


**Figure 2.** NMO and NTP equilibrium potentials used in the present simulations. These curves were extrapolated from absolute potentials measured experimentally during charge and discharge of an NTP/NMO cell at 0.6 C in Ref. 38. Data points show the conditions that electrodes in NTP and NMO cells were initialized with in all simulations.

where  $R_g$ ,  $T$ , and  $F$  are the universal gas constant, temperature (here, 298 K), and Faraday's constant, respectively. The exchange-current density  $i_0$  for intercalation reactions<sup>40</sup> depends on salt concentration in the electrolyte  $c_e$ , the number of cations formed from dissociation of one salt molecule  $s_+$ , the fraction  $x_{Na}$  and the terminal concentration  $c_{s,max}$  of intercalated Na in electroactive particles, and the kinetic rate-constant  $k$ :

$$i_0 = Fkc_{s,max}(s_+c_e)^{0.5}(1-x_{Na})^{0.5}(x_{Na})^{0.5}. \quad [2]$$

Since no direct measurements of Na-ion intercalation kinetics exist in the literature for NTP and NMO (to our knowledge), we fit experimental polarization data at several C-rates (from Ref. 38) to the predictions of our model by adjusting the rate constant for NTP and NMO independently, the outcomes of which are described in the next sub-section. From this procedure we found NTP and NMO to have Na-intercalation rate-constants of  $6.31 \times 10^{-13}$  and  $2.12 \times 10^{-11}$  mol/m<sup>2</sup>-s per (mol/m<sup>3</sup>)<sup>1.5</sup>, respectively.

The fraction of intercalated Na inside solid electroactive-particles increases when intercalation reactions occur with the electrolyte. The intercalated-Na fraction can vary throughout the electroactive particles. However, due to the large Na-ion diffusivity in NMO and NTP (greater than  $10^{-16}$  m<sup>2</sup>/s in NTP<sup>38</sup> and between  $1 \times 10^{-17}$  and  $9 \times 10^{-16}$  m<sup>2</sup>/s in NMO<sup>41</sup>), this variation is less than 10% in both NTP and NMO (based on formulas derived in Ref. 42). Consequently, we neglect this effect. Intercalated-Na fraction  $x_{Na}$  (at a particular point inside a given electrode) evolves with time (according to mass conservation) as a result of intercalation current-density  $i_n$  at electroactive-particle surfaces:

$$v_s c_{s,max} \frac{\partial x_{Na}}{\partial t} + av_s \frac{i_n}{F} = 0, \quad [3]$$

where  $a$  and  $v_s$  are the volumetric surface area and volume fraction of electroactive particles in the porous electrode, respectively. The volumetric surface area of electroactive particles is  $5.73 \times 10^6$  m<sup>-1</sup> and  $2.14 \times 10^7$  m<sup>-1</sup> for NMO and NTP respectively (assuming spherical particles whose size was measured in Ref. 38).

Na ions are removed from flowing electrolyte as Na intercalates into electroactive particles. Thus, balance of species must be accounted for in a desalination device to preserve solution-phase electroneutrality. We model flow of electrolyte through porous electrodes (containing electroactive particles, electronically conductive carbon, and polymeric binder) using Darcy's Law. When the fluid permeability of the separator/membrane is neglected, the superficial-velocity of electrolyte  $\vec{v}_s$  is uniform and one-dimensional (i.e.,  $\vec{v}_s = u_s \hat{i}$ ). For the present binary electrolyte we model the transport of Na<sup>+</sup> and Cl<sup>-</sup> using dilute-solution theory that is cast in terms of the solution-phase potential  $\phi_e$  of the cation (here, Na<sup>+</sup>) and salt concentration  $c_e$ . Salt conservation in the electrolyte can be described by a potential-independent equation for binary electrolytes<sup>37</sup>:

$$\varepsilon \frac{\partial c_e}{\partial t} + \vec{v}_s \cdot \nabla c_e + \nabla \cdot (-D_{eff} \nabla c_e) - av_s (1-t_+) \frac{i_n}{s_+ F} = 0. \quad [4]$$

Salt concentration inside of each electrode is assumed to be uniform initially with the same concentration as the influent solution (that is chosen based on the specific operating conditions investigated). The rightmost term in Eq. 4 is the local rate of salt accumulation (in mol/L-s) that is driven by exchange of Na ions between electroactive particles and electrolyte. This rate is affected by the Na-intercalation current-density  $i_n$ , volumetric surface area of electroactive particles  $a$ , their volume fraction  $v_s$ , and the electrolyte's Na-ion transference number  $t_+$ . Equation 4 assumes a concentration-independent transference number for Na ions  $t_+$  of 0.39 (from the dilute-limit value), which deviates by less than 10% in concentrated solutions.<sup>43</sup>  $D_{eff}$  is the effective salt diffusivity, which is reduced from the bulk value  $D_0$  (taken as  $1.61 \times 10^{-9}$  m<sup>2</sup>/s for dilute NaCl<sup>37</sup>) by a factor  $D_{eff}/D_0 = \varepsilon^{1.5}$  (assuming Bruggeman scaling) that depends on porosity of the electrode  $\varepsilon$ . Here, we neglect the effect of pore-scale dispersion on apparent diffusion through the porous electrode (assuming small pore-scale Peclet number<sup>44</sup>).

Charge transport in the electrolyte is governed by current conservation:<sup>37</sup>

$$\nabla \cdot \left[ -\kappa_{eff} \left( \nabla \phi_e - \frac{2R_g T}{F} (1-t_+) \nabla \ln c_e \right) \right] - av_s i_n = 0, \quad [5]$$

where  $\kappa_{eff}$  is the effective ionic conductivity that depends on the corresponding bulk value  $\kappa_0$  and porosity as  $\kappa_{eff} = \varepsilon^{1.5} \kappa_0$  (assuming Bruggeman scaling). Here, the local ionic current-density is  $\vec{i}_e = -\kappa_{eff} (\nabla \phi_e - (2R_g T/F)(1-t_+) \nabla \ln c_e)$ . We use experimental data<sup>45</sup> to model the dependence of bulk ionic-conductivity on salt concentration.

When a Na-blocking membrane is used to isolate the two electrodes, boundary conditions must be expressed on its opposing sides (labeled here as + and - for cathode and anode sides, respectively). We impose a Neumann condition on the solution-phase potential at these boundaries (i.e.,  $-\hat{n} \cdot \nabla \phi_e = 0$ , where  $\hat{n}$  is the outward-pointing unit-normal for a given side of the membrane) to enforce null Na-ion transport through an ideal perm-selective membrane. This condition is equivalent to a null-flux condition on cation transport because the solution-phase potential is proportional to the electrochemical potential of the cation that is the driving force for diffusive and migrational transport of the cationic species (see Ref. 46).

Additionally, solution-phase potential is not continuous across the membrane because concentration polarization is produced by the difference in salt concentration inside electrolyte between opposing sides of the membrane. Assuming that the perm-selective membrane is close to equilibrium, the drop in electrostatic potential across the membrane (from cathode to anode) is given by<sup>47</sup>  $\phi_{ES,+} - \phi_{ES,-} = R_g T/F \ln(c_{e,-}/c_{e,+})$ . The solution-phase potential  $\phi_e$  represents the reduced electrochemical-potential of the cationic species Na<sup>+</sup> (see Ref. 46), which is defined as<sup>37</sup>  $\phi_e = \phi_{ES} + R_g T/F \ln(c_e)$ . Using this relationship we find that the solution-phase potential-drop across the membrane is twice that of the electrostatic potential  $\phi_{e,+} - \phi_{e,-} = 2R_g T/F \ln(c_{e,-}/c_{e,+})$ . Accounting for potential drop in this way is necessary for accurate modeling of the thermodynamic limit of desalination for a device using a membrane. When a porous separator is used to isolate anode and cathode, we neglect the separator's thickness and permeability, in which case Eqs. 4 and 5 are continuously differentiable across the separator and do not require additional boundary conditions. Current-collector and outflow boundaries are modeled as impenetrable to ionic diffusion and migration, and consequently null-flux conditions are applied to diffusive salt transfer and ion current on these boundaries (i.e.,  $-\hat{n} \cdot D_{eff} \nabla c_e = 0$  and  $\hat{n} \cdot \vec{i}_e = 0$  on the boundary whose outward-pointing unit-normal is  $\hat{n}$ ). At inflow boundaries a constant-concentration (i.e., Dirichlet) condition is imposed to account for salt diffusion between the cell and the reservoir that feeds saline water to it. We impose null ionic-current on such boundaries, as though an insulator were placed between the influent streams feeding the two electrodes so as to eliminate shunt currents (see Ref. 48) between them.

Finally, electron conduction to and from the external circuit into the composite electrodes is necessary to make the cell operate. The current collectors that adjoin the respective electrodes are assumed to have uniform solid-phase potentials ( $\phi_{s,+}$  and  $\phi_{s,-}$  are used to denote the solid-phase potential of cathode and anode current collectors, respectively). Cell voltage (defined as  $V_{cell} = \phi_{s,+} - \phi_{s,-}$ ) is adjusted to maintain the average current-density  $i$  applied to the current collector at a specified time-independent value (i.e., galvanostatic conditions are imposed) while the anode solid-phase potential  $\phi_{s,-}$  is grounded at 0 V. Separators and membranes are considered perfect electronic insulators. Solid-phase potential variations inside the porous electrode are governed by current conservation:

$$\nabla \cdot (-\sigma_s \nabla \phi_s) + av_s i_n = 0, \quad [6]$$

where  $\sigma_s$  is the effective electronic conductivity of the heterogeneous electrode. Here, we take a value of 100 S/m that results in small solid-phase potential variations relative to that of the solution-phase potential in the electrolyte. This value is reasonable, considering that

Li-ion porous-electrode films can be fabricated with effective electronic conductivity of 20–400 S/m depending on binder and carbon content.<sup>49</sup> Further, ohmic polarization inside the cell is dominated by bulk ionic-transport resistance when effective electronic-conductivity exceeds the effective ionic-conductivity (here, 1.6 S/m at 700 mol/m<sup>3</sup> salt concentration with 40% porosity). We show later that the results are insensitive to the choice of effective electronic-conductivity.

**Numerical discretization, model implementation, and validation.**—The coupled modeling equations were discretized using the finite-volume method. A first-order implicit scheme was used to integrate in time, while a second-order central-difference scheme was used for non-convective flux and a first-order upwind-difference scheme was used for convective flux. An algorithm used previously to simulate suspension flow-batteries<sup>50</sup> was modified for use in desalination simulations by (1) incorporating electrolyte potential and concentration variations, (2) anchoring solid parts of the porous electrode, and (3) incorporating continuous flow of the liquid-phase electrolyte. We note that non-linearity of the discrete governing equations requires iteration to obtain a converged solution at a given time step. Here, we employ a sequence of iteration loops to solve the non-linear system of equations (as described in Ref. 51), where electrolyte conductivity is resolved in the outer loop, electrochemical kinetics are resolved in the inner loop, and the aggregation-based algebraic multigrid method<sup>52–55</sup> is used as a linear solver.

The present model builds on a Li-ion battery model without electrolyte flow and whose solution-phase potential, solid-phase potential, and salt concentration fields were validated<sup>51</sup> by comparison with those predicted by the Dualfoil 5 program (Refs. 56,57). The present model captures additional transport processes, including (1) anion-selective membrane transport and membrane polarization, (2) continuously flowing electrolyte, and (3) Na-ion intercalation. To verify implementation and confirm the physical consistency of these additional model features, output predictions were compared with idealized, analytical models. Firstly, a symmetric-NMO cell with a membrane was simulated with stationary electrolyte disconnected from electrolyte reservoirs. The electrodes for these cells were chosen with 1 mm thickness, 20 mm length, 40 vol.% porosity, and 50 vol.% NMO loading. Under these conditions, transient salt-depletion occurs in one electrode while the opposing electrode concentrates simultaneously. Salt concentration and average membrane-polarization simulated at  $5 \times 10^{-5}$  C differed respectively by  $10^{-6}\%$  and 0.2% from the values expected based on average concentrations predicted by Faraday's Law ( $\bar{c}_e(t) = c_e^0 \pm it/wF\varepsilon$ , where  $c_e^0$  is the initial concentration). After 5 hours of charging at  $5 \times 10^{-5}$  C the concentration profile in the  $x$ -direction differed by  $10^{-5}\%$  from that expected from a pseudo-steady solution of Eq. 4 with uniform intercalation current-density ( $c_e(x, t) = c_e^0 \pm i(t/\varepsilon + t_+(x^2 - w^2/3)/2D_{eff})/wF$ ). The same cell was simulated with electrolyte connected to a stationary electrolyte-reservoir at its inlet. When cycled at  $5 \times 10^{-6}$  C, both electrodes showed salt-concentration distributions in the  $y$ -direction that differed by less than 0.04% from those expected from a thickness-averaged, steady solution of Eq. 4 with uniform intercalation current-density and with membrane current-density localized at the inlet ( $c_e(y) = c_e^{in} \pm iy(L - 0.5y)(1 - t_+)/2wFD_{eff}$ , where  $c_e^{in}$  is the inlet concentration). With flowing electrolyte at a superficial velocity of 22  $\mu\text{m/s}$ , the time-averaged effluent-concentration in the

desalinated electrode differed by 1% from that predicted by Faraday's Law when cycled at C/2 rate ( $\bar{c}_e^{out} = c_e^{in} \pm iL/wF\varepsilon u_s$ ).

We fitted the model predictions of individual-electrode polarization at 6 C and 12 C for an asymmetric NMO/NTP cell with aqueous Na<sub>2</sub>SO<sub>4</sub> electrolyte to experimental data<sup>38</sup> to estimate the kinetic rate-constants of NTP and NMO Na-ion intercalation. No other adjustable parameters were fitted. As Table I shows, the model produced polarization levels within 20% of the experimental values between 6 C and 12 C on both electrodes, i.e., this accuracy was obtained by fitting four polarization values with two kinetic parameters. Experimental polarization at 0.6 C (from Ref. 38) was not compared to the model because cycling at that rate produced low experimental coulombic efficiency ( $\sim 90\%$ ) relative to that of 6 C and 12 C ( $>98\%$ ), suggesting that side reactions affect cycling substantially at that rate. We note also that the charge capacities predicted between 6 C and 12 C exceed experimental values by 20–30 mAh/g-NTP (the experimental capacity was 104 mAh/g-NTP at 6 C versus a modeled capacity of 126 mAh/g-NTP). This discrepancy is not unexpected considering that the present model neglects the effects of side reactions and electroactive-material decomposition that have been reported for experimental NIBs using aqueous electrolyte.<sup>20,38</sup> Holding to an optimistic outlook for the development of aqueous NIBs with long cycle-life (in which side and decomposition reactions have been mitigated), the present model optimistically predicts the performance of NID cells.

## Results and Discussion

The development of efficient NID cells requires a careful choice of materials and dimensions used in the cell's construction. Additionally, the electrochemical-cycling and flow conditions used to operate the cell will affect its performance in a given application. We assess these aspects of cell development firstly by examining how galvanostatic cycling is affected by the choices of Na intercalant and the type of membrane or separator between the two electrodes. We then test the effect of average applied current-density and electrode thickness on cell-cycling performance, which were obtained for 700 mM-NaCl influent and 50% water recovery. Unless otherwise specified, each simulated cell has 1 mm electrode thickness and 20 mm current-collector length, and the volume fraction of electroactive-material loading was fixed to 50 vol.% (producing areal capacities of 10.2 mAh/cm<sup>2</sup> for NMO and 16.1 mAh/cm<sup>2</sup> for NTP) with 40 vol.% porosity (binder and conductive-additive accounted for in the balance of electrode volume). Finally, we show that optimized cells can be cycled efficiently with influent concentrations ranging between brackish water and seawater and with water recovery up to 95%. We quantify electrochemical performance in each case based on the following metrics:

- The desalination energy  $E_d$  is calculated as the average energy consumed per unit volume of desalinated water as  $E_d = L \int V_{cell} i dt / u_{s,d} \varepsilon w \Delta t$ , where  $i$  is the space-averaged, applied current-density at a given instant in time,  $L$  is the length of the cell along the flow direction,  $w$  is the electrode thickness,  $u_{s,d}$  the superficial velocity of desalinated water, and  $\Delta t$  is the elapsed time.
- The time-averaged polarization  $\Delta\bar{\Phi}$  is calculated as  $0.5(\bar{V}_{cell,C} - \bar{V}_{cell,D})$ , where  $\bar{V}_{cell,C}$  and  $\bar{V}_{cell,D}$  are the time-averaged voltages on charge and discharge, respectively.
- The degree of desalination  $s$  is calculated as  $s = (c_e^{in} - \bar{c}_{e,desal}^{out}) / c_e^{in}$ , where the influent salt concentration is  $c_e^{in}$  and the

**Table I.** Comparison of polarization predicted by the present model with previous experiments<sup>38</sup> on an NMO/NTP cell in aqueous Na<sub>2</sub>SO<sub>4</sub> electrolyte.

Rate	Cathode Polarization (mV)		Anode Polarization (mV)		Total Polarization (mV)	
	Simulation	Experiment	Simulation	Experiment	Simulation	Experiment
6 C	29	35	125	145	154	180
12 C	54	50	191	195	245	245

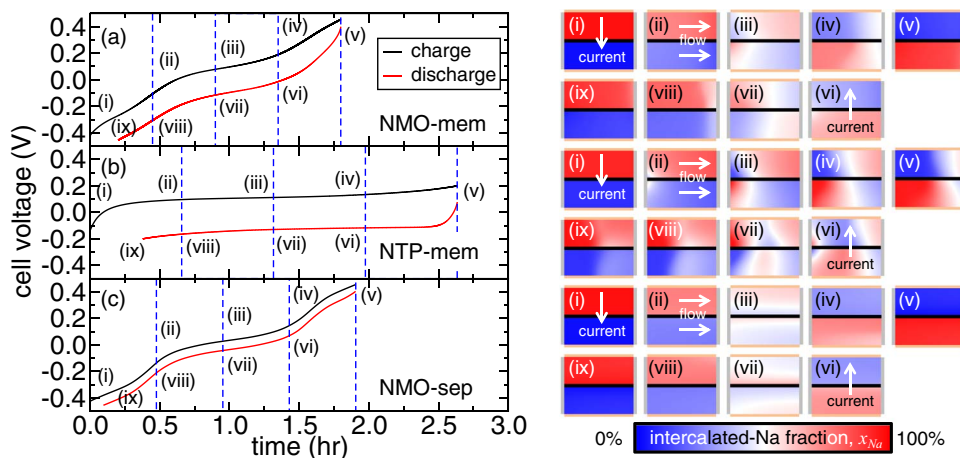


**Figure 3.** Cell voltage as a function of time (left) during the first charge/discharge cycle of (a) NMO-membrane cell, (b) NTP-membrane cell, and (c) NMO-separator cell. At indicated instants in time (i-ix) the the distribution of intercalated Na in electroactive particles is shown (right).

time- and space-averaged salt concentration of the desalinated effluent is  $\bar{c}_{e,desal}^{out}$ .

- The utilization  $\chi$  of electroactive-material charge-capacity is calculated as the time for a galvanostatic process to complete  $\Delta t$  (between a specified window of cell-voltage cutoffs) relative to the ideal time  $\Delta t_{ideal}$ , which is determined by a cell's theoretical capacity and the current applied to it.

**Electrochemical processes during cell cycling.**—Three types of symmetric Na-intercalation cells were simulated here with an average applied current density of 51 A/m<sup>2</sup>: (1) NMO electroactive material with a Na-blocking membrane, (2) NTP electroactive material with a Na-blocking membrane, and (3) NMO electroactive material with a porous separator that is not ion-selective. The targeted degree-of-desalination is 68%. A charge balance on the cell shows that achieving the 68% desalination target requires a pore-scale mean-velocity (i.e., the product of porosity and superficial velocity) of 56  $\mu\text{m/s}$ , which corresponds to an intra-cell water residence-time of 360 seconds. Hence NMO cells, with a C-rate of 0.5 hr<sup>-1</sup>, theoretically allow a net desalinated-water output that is 20 times the open-pore cell volume during each charge/discharge cycle. The same flow velocity was used in both electrodes to maintain 50% water recovery.

Figure 3 shows the variation of cell voltage for the three cells of interest. The distribution of intercalated Na is shown at nine instants in time as well. Initially, electroactive particles in the cathode and anode, respectively, are concentrated with and depleted in intercalated Na (snapshot i in Figs. 3a–3c). This produces a negative cell voltage initially because equilibrium potential of a given electroactive material decreases with increasing intercalated-Na fraction, which requires each cell to operate in a mode where energy is recovered from the cell rather than delivered to it. As we show later, the net energy consumed will depend on the efficiency with which energy is recovered. Cell voltage increases during charging, becoming positive after a certain period of time that depends on the type of electroactive material used (NMO or NTP here). Charging stops once the cutoff cell-voltage is reached (chosen as 0.455 V for NMO and 0.200 V for NTP). For the NMO cells (Figs. 3a and 3c) nearly complete utilization of electroactive-material capacity is obtained (snapshot v), while electroactive material at the outlet of the NTP cell is underutilized at the end of the charge cycle (Fig. 3b, snapshot v). Despite this, the NTP cell cycles for a longer period of time (2.8 hr for NTP versus 1.9 hr for NMO) because NTP produces a higher areal capacity (16.1 mAh/cm<sup>2</sup>) than NMO (10.2 mAh/cm<sup>2</sup>).

When the direction of current is reversed, the cell begins to discharge current from the cathode and cell voltage decreases. Discharging stops once the low-potential cutoff-voltage is reached (−0.455 V for NMO and −0.200 V for NTP). The gap between the charge (black)

and discharge (red) cell-voltage curves is equal to twice the cell polarization, which is a measure of the net amount of energy required to desalinate (without energy recovery losses). Among the three cells simulated, the NTP-Membrane cell shows the highest cell-level polarization, followed by the NMO-Membrane cell. The NTP-Membrane cell has highest polarization due to the low reaction rate-constant of NTP. Snapshots i-ix in Figs. 3a and 3b show that a reaction zone propagates from the inlet to the outlet in the two cells having Na-blocking membranes, while a separator allows for more uniform intercalation of Na.

Though the NMO-Separator cell shows lowest polarization and highly uniform reactions, these improvements occur with low degree-of-desalination. These results show that a Na-blocking membrane must be used to achieve high degree-of-desalination. Figure 4 shows the time variation of effluent salt-concentration (or salinity in mol/L) in the concentrated and diluted electrodes. Also, the distribution of salinity inside each electrode is shown at several instants in time. Initially salt concentration changes uniformly inside each electrode (before snapshot ii), but eventually the membrane-based cells in Figs. 4a and 4b (using NMO and NTP, respectively) show steady effluent salt-concentrations and exhibit near-theoretical degree of desalination based on charge counting (65%). The Na-blocking membrane enables highly concentrated salt-solution to persist in the outlet of the cell without diffusing across the membrane (Figs. 4a and 4b, snapshots ii and iii). In contrast, the NMO-Separator cell (Fig. 4c) shows only 25% degree-of-desalination. The separator-based cell achieves less than half the theoretical degree-of-desalination because the separator allows salt to diffuse from the concentrated electrode into the diluted electrode.

The robustness of the present results was confirmed by simulating the sensitivity of desalination performance to the values assumed for the effective electronic conductivity  $\sigma_e$  of the porous electrodes and the kinetic rate-constant  $k$  for Na intercalation. Table II shows that the energy consumed during desalination (with lossless energy recovery) by NTP and NMO cells (using membranes) increases by 2% when electronic conductivity is reduced one order of magnitude from 100 S/m to 10 S/m. Also, electroactive-material utilization decreases by less than 1% from 100 S/m to 10 S/m. These results indicate that the predictability of the present simulations is not limited by variations in effective electronic-conductivity that could result from electrode processing. Table III shows that desalination energy for both cells decreases by 4–9% when the kinetic rate-constant increases by one order of magnitude from the value fitted to experimental polarization. Thus, the present results are indicative of electroactive materials with facile intercalation kinetics. Reducing the rate constant by an order of magnitude produces 43% and 98% higher desalination energy for NMO and NTP cells, respectively. While the NMO cell is able to

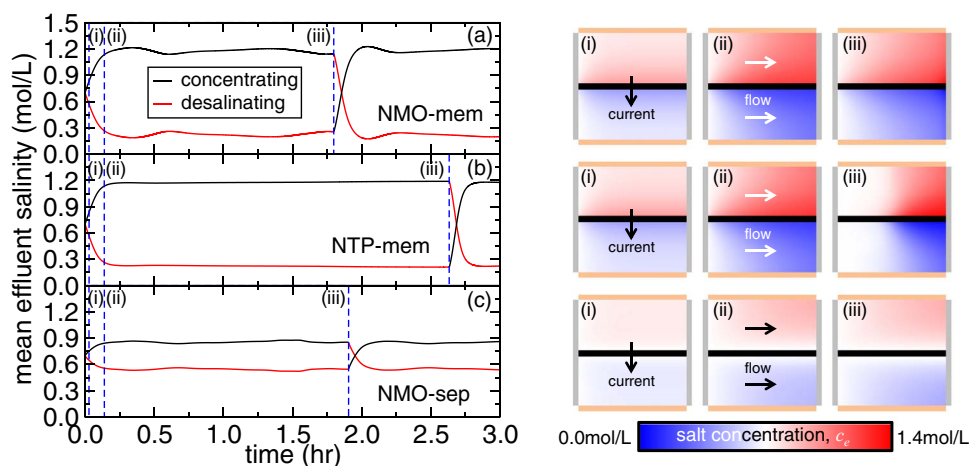


**Figure 4.** Space-averaged outlet salt-concentration in the electrolyte (left) during the charge cycle of a (a) NMO-membrane cell, (b) NTP-membrane cell, and (c) NMO-separator cell. At the indicated instants in time (i-iii) the distribution of NaCl in the electrolyte is shown (right).

**Table II.** Desalination energy and utilization on discharge as a function of effective electronic conductivity for the conditions and parameters simulated in Figs. 3 and 4. The bold line lists the results for the effective electronic conductivity assumed for all subsequent results.

$\sigma_s$ S/m	NMO-Membrane		NTP-Membrane	
	Desalination Energy kWh/m <sup>3</sup>	Utilization %	Desalination Energy kWh/m <sup>3</sup>	Utilization %
1000	1.23	80.0	1.64	69.3
<b>100</b>	<b>1.23</b>	<b>79.9</b>	<b>1.65</b>	<b>69.3</b>
10	1.26	79.3	1.67	69.0
1	1.63	73.6	1.90	62.7

achieve substantial utilization (74%), the NTP cell does not function effectively with such low rate constants, achieving less than 1% utilization. Thus, facile intercalation kinetics are needed for NID cells to function.

A critical consideration in the design of NID cells is the electrochemical stability window of water, because a stable electrolyte will enable efficient, reversible cycling. Reduction potentials range between 0.35 to 0.80 V vs. SHE inside NMO-Membrane cells and  $-0.62$  to  $-0.40$  V vs. SHE inside NTP-Membrane cells for the cases shown in Figs. 3 and 4.  $O_2$  evolution occurs for neutral pH at potentials higher than 0.81 V vs. SHE, and  $H_2$  evolution occurs at potentials less than  $-0.41$  V vs. SHE. Seawater pH is slightly basic, with a pH of about 8.<sup>58</sup> Therefore,  $O_2/H_2$  evolution is unlikely to occur during cycling of NMO-based cells when seawater is desalinated. In contrast, NTP-based cells will likely evolve  $H_2$  in seawater unless pH exceeds 11.5. Also, we note that previous experiments<sup>20</sup> suggest that NTP decomposition occurs in alkaline solutions with pH > 9, and this effect may require use of NTP cells outside of the electrolyte stability-window. We note that the present model does not account for the mechanism of electroactive-material mediated hydrolysis believed to

occur with other aqueous electroactive materials,<sup>38</sup> and experimental investigation is needed to assess these effects. Also, the concentration and dilution of salt could induce a shift in pH inside the cell and that effect has not been accounted for presently.

**Effect of current density and electrode thickness.**—When a Na-ion cell with a Na-blocking membrane is used to desalinate water, the rate at which desalination occurs is affected by a variety of parameters. High current densities can be used to desalinate water at high throughput rates by increasing flow rate in proportion to current density. Also, the cost of a Na-ion cell decreases as electrode thickness increases because the fraction of cost from inactive cell components (e.g., membranes and current collectors) is reduced with cells having thick electrodes. Therefore, understanding the effects of current density and electrode thickness on desalination performance will enable the design and operation of low-cost, efficient desalination devices.

We first investigate the effect of applied current-density on desalination performance (Fig. 5). Among the different current densities tested, the water flow-rate was varied in proportion with current density, so as to maintain the same theoretical degree-of-desalination expected from Faraday's Law. For influent seawater with 700 mM NaCl, the present cases are expected to achieve 224 mM salinity in the depleted stream (68% degree-of-desalination). For both NTP and NMO cells, current densities below 77 A/m<sup>2</sup> produce salinity levels less than 260 mM on average in the depleted stream (63% degree-of-desalination), which is near the 68% theoretical degree-of-desalination (Fig. 5b). For the lowest current density simulated (5 A/m<sup>2</sup>) the desalination energy needed with lossless energy recovery exceeds the thermodynamic minimum (0.49 kWh/m<sup>3</sup>, see Ref. 59) by 32% for NMO and 58% for NTP. While energy recovery has negligible impact on NTP cells (due to the large range of intercalation over which equilibrium potential is constant as shown in Fig. 2), NMO cells cycled at low current density require twice as much energy when energy recovery is not utilized. We also observe that the utilization of electroactive-material charge-capacity decreases with

**Table III.** Desalination energy and utilization on discharge as a function of kinetic rate-constant for the conditions and parameters simulated in Figs. 3 and 4. The bold line lists the results for the rate constants assumed for all subsequent results.

Rate Constant mol/m <sup>2</sup> -s per (mol/m <sup>3</sup> ) <sup>1.5</sup>	NMO-Membrane		NTP-Membrane	
	Desalination Energy kWh/m <sup>3</sup>	Utilization %	Desalination Energy kWh/m <sup>3</sup>	Utilization %
$2.12 \times 10^{-10}$	1.18	81.1	$6.31 \times 10^{-14}$	71.0
<b><math>2.12 \times 10^{-11}</math></b>	<b>1.23</b>	<b>79.9</b>	<b><math>6.31 \times 10^{-13}</math></b>	<b>69.3</b>
$2.12 \times 10^{-12}$	1.76	70.8	$6.31 \times 10^{-12}$	0.001

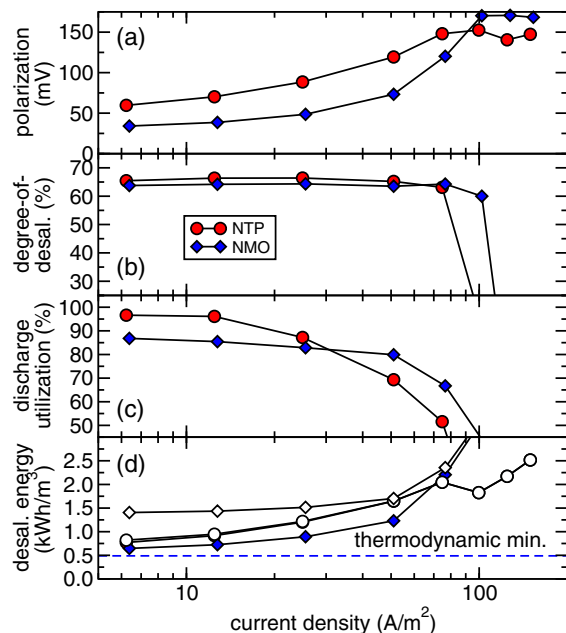


**Figure 5.** Desalination performance as a function of current density for NMO and NTP cells that use Na-blocking membranes. From top to bottom: (a) time-averaged polarization, (b) degree-of-desalination on discharge, (c) discharge utilization, and (d) desalination energy on discharge. The dashed line indicates thermodynamic minimum energy. Filled and white symbols represent 100% and 0% energy recovery, respectively.

increasing current density (Fig. 5c). At high current densities polarization (Fig. 5a) causes cell voltage to reach the pre-specified voltage cutoff value earlier in both the charge and discharge processes. When this occurs, a smaller amount of water is desalinated during a complete cycle and is manifested as decreased utilization (less than 50%) at current densities higher than  $77 A/m^2$ . Also, the desalination energy (in  $kWh/m^3$ , Fig. 5d) varies dramatically for current densities in this range:  $0.7\text{--}0.9 kWh/m^3$  is needed to desalinate at  $13 A/m^2$ , while  $2.0\text{--}2.2 kWh/m^3$  is needed to desalinate at  $77 A/m^2$ . High current densities enable rapid production of desalinated water (since flow velocity is proportional to the current density), but the energy required to produce it may dictate use of lower current densities. Also, NTP cells show higher polarization than NMO cells at the same current density, which is consistent with the results in Figs. 3 and 4. NTP cells show higher kinetic polarization due to its lower kinetic rate-constant compared to NMO ( $6.31 \times 10^{-13}$  versus  $2.12 \times 10^{-11}$   $mol/m^2\cdot s$  per  $(mol/m^3)^{1.5}$ ).

As mentioned previously, electrode thickness will affect the cost of an NID cell. Therefore, it is desirable to understand how design changes to this dimension will affect cell performance. When the C-rate is held constant among different electrode thicknesses, the theoretical time-scale for charge and discharge is held constant among all cases. Figure 6 shows the desalination performance for various electrode thicknesses simulated at 0.25 C, 0.50 C, and 1.00 C rate (corresponding to theoretical charge times of 4 hr, 2 hr, and 1 hr, respectively). In addition the pore-scale mean-velocities were set to 28  $\mu m/s$ , 56  $\mu m/s$  and 111  $\mu m/s$  for 0.25 C, 0.50 C, and 1.00 C, so as to achieve 68% theoretical degree-of-desalination in all cases.

For a given C-rate, cell polarization increases quadratically with electrode thickness (Fig. 6a) due to the dominant role of ohmic drop through the electrolyte, limiting the degree-of-desalination, utilization, and efficiency of thick electrodes (Figs. 6b–6d). At 0.25 C, 0.50 C, and 1.00 C, thicknesses of 0.75 mm, 1.25 mm, and 1.75 mm (respectively) operate with 70% utilization and 60% degree-of-desalination, but require three times the minimum desalination-energy expected from thermodynamics even with lossless energy-recovery. In contrast, thicknesses of 250  $\mu m$ , 500  $\mu m$ , and 750  $\mu m$  can desalinate within 50% of the thermodynamic minimum ( $0.72\text{--}0.74 kWh/m^3$ )

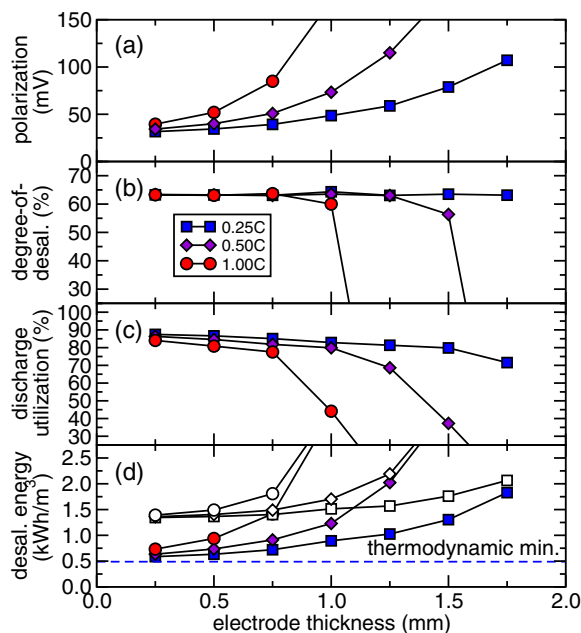


**Figure 6.** Desalination performance as a function of electrode thickness for the NMO-membrane cell for C/4, C/2, and 1 C rates. From top to bottom: (b) time-averaged polarization, (c) degree-of-desalination on discharge, (d) discharge utilization, and (e) desalination energy on discharge. The dashed line indicates thermodynamic minimum energy. Filled and white symbols represent 100% and 0% energy recovery, respectively.

when cycled at 0.25 C, 0.50 C, and 1.00 C with lossless energy-recovery, respectively.

**Effect of influent salinity and water recovery.**—The specific application for which a desalination device is used dictates the salt concentration of the influent and the amount of effluent concentrate that is tolerable. Therefore, we predict the desalination performance that can be achieved when using water sources with influent salinity ranging from levels of typical brackish water (70 mM) up to those of typical seawater (700 mM). Though moderate levels of water recovery are acceptable when potable water is processed from abundant sources, higher water-recovery is required where influent feed-water is scarce. Accordingly, we predict that Na-ion cells can achieve high water-recovery by simulating desalination performance for 50–95% water-recovery levels.

Figure 7 shows desalination performance as a function of influent salt-concentration. In each cell, C-rate was reduced in proportion with influent salt-concentration (Fig. 7a) because brackish water has lower ionic conductivity than seawater and, consequently, cells operating with brackish influent will have lower rate capability than those operating with seawater. Among the influent concentrations simulated, influent velocity was varied so as to achieve 68% theoretical degree-of-desalination. Both 1.00 mm- and 0.50 mm-thick electrodes were simulated at each influent concentration. For a given thickness, polarization, degree-of-desalination, and electroactive-material utilization varied by less than 5 mV, 5%, and 1%, respectively, among the different influent concentrations (Figs. 7b–7d). While the aforementioned performance metrics are invariant with influent salinity, desalination energy decreases as influent concentration decreases (Fig. 7e) because the amount of charge-transfer (in coulombs per  $m^3$  of solution) required to achieve a certain degree-of-desalination decreases with influent salinity. For 1.00 mm-thick electrodes desalination energy was 2.5 times the thermodynamic minimum-energy with lossless energy-recovery (Fig. 7e), but desalination energy decreases to within 40% of the thermodynamic minimum for 0.50 mm-thick electrodes (Fig. 7e).

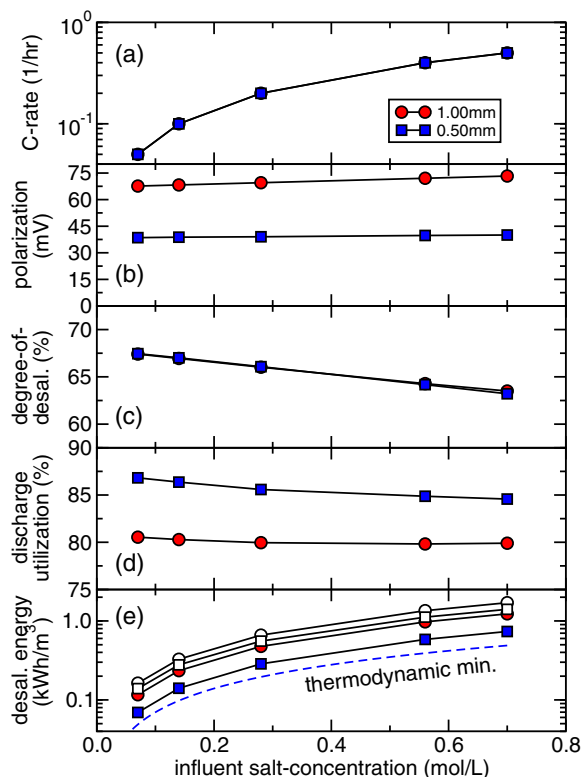


**Figure 7.** Desalination performance as a function of influent concentration for the NMO-membrane cell for 1.00 mm- and 0.50 mm-thick electrodes. From top to bottom: (a) choice of C-rate, (b) time-averaged polarization, (c) degree-of-desalination on discharge, (d) discharge utilization, and (e) desalination energy on discharge. Filled and white symbols represent 100% and 0% energy recovery, respectively.

Water recovery  $r$  is defined as the fraction of desalinated water-volume relative to influent water-volume. The symmetric cells simulated here are designed with equal cathode and anode electrode thicknesses (i.e.,  $w_a = w_c$ ). Therefore, water recovery  $r$  increases as superficial velocity  $u_{s,d}$  in the depleting electrode (anode on charge, cathode on discharge) increases and as superficial velocity  $u_{s,a}$  in the accumulating electrode (cathode on charge, anode on discharge) decreases, according to the following relationship  $r = u_{s,d}/(u_{s,d} + u_{s,a})$ . To adjust water recovery we reduce the superficial velocity in the accumulating electrode and keep the superficial velocity in the depleting electrode constant (Fig. 8a). When charging stops and discharging starts, the direction of current is switched. Consequently, superficial velocities in the respective electrodes are swapped. In an experimental device, appropriate plumbing will be required to achieve these flow conditions. Cell performance is shown in Fig. 8 as a function of water recovery for 700 mM and 70 mM influent concentrations. For both influents, polarization and desalination energy (Figs. 8b,8d) increase mildly with water recovery due to the increase in Donnan potential resulting from the high salt-concentrations produced at high water recovery. We note also that the desalination energy with lossless energy-recovery for high water-recovery levels exceeds the thermodynamic minimum by a lesser amount (84%) than with 50% water-recovery.

With 700 mM influent the degree-of-desalination decreased from 65% to 30% between water-recovery levels of 80% and 95% (Fig. 8c). This effect results from the discharge process beginning with residual concentrated solution from the charge process. This effect is illustrated in Fig. 9a, which shows the variation of effluent concentration with time for 700 mM influent with 80% water recovery. Immediately following completion of the charge process (1.75 hr), the discharge process commences with an effluent concentration (2 mol/L) far in excess of the inlet concentration (0.7 mol/L).

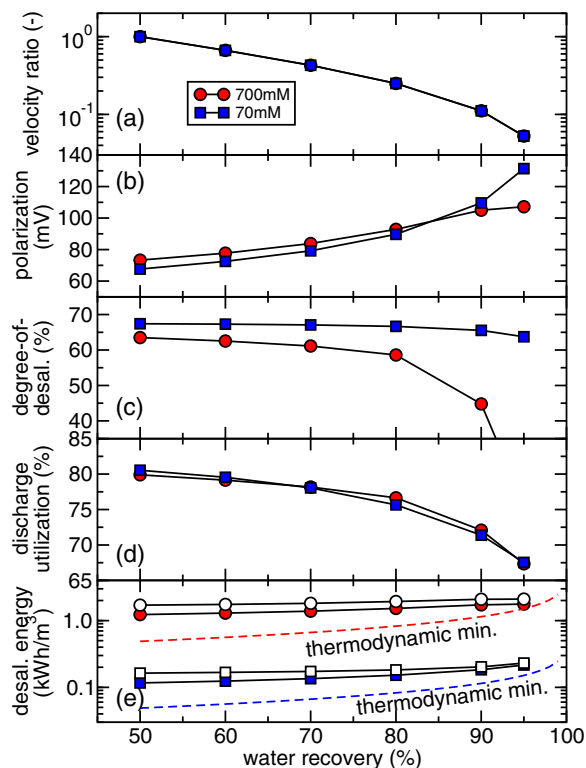


**Figure 8.** Desalination performance as a function of water recovery for the NMO-membrane cell with 700 mM-influent cycled at C/2 and 70 mM-influent cycled at C/20. Data are shown for two cycling scenarios where the cell was cycled with and without influent purging between charge and discharge, as explained in the text. From top to bottom: (a) ratio of concentrating- and desalinating-electrode velocities, (b) time-averaged polarization, (c) degree-of-desalination on discharge, (d) discharge utilization, and (e) desalination energy on discharge. Filled and white symbols represent 100% and 0% energy recovery, respectively.

Desalination of residual NaCl delays production of desalinated effluent with the target concentration (224 mM) by 30 minutes, which constitutes a substantial fraction of the entire discharge process (1.5 hours). For higher water-recovery levels this effect becomes more significant. In addition effluent concentrations in excess of the NaCl solubility limit were predicted at 90% water-recovery. For lower levels of water recovery the degree-of-desalination can be enhanced by purging the cell with fresh effluent immediately following a charge or discharge step.

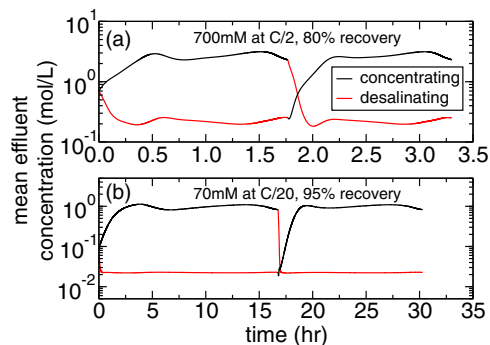


**Figure 9.** Mean effluent concentration as a function of time for the NMO-membrane cell with (a) 700 mM-NaCl influent cycled at C/2 with 80% water recovery and (b) 70 mM-NaCl influent cycled at C/20 with 95% water recovery.

In contrast, cells cycled with 70 mM influent sustained degrees-of-desalination levels of greater than 64% for water recovery levels as high as 95%. The transient effluent-concentration in 70 mM cells exhibits similar effects due to residual NaCl that are similar to those in 700 mM cells, but the time delay to production of target concentrations is very short (<30 min) relative to the total discharge time (15 hr). Furthermore, the maximum effluent-concentration reached during the entire charge/discharge process at 95% water recovery (~1 mol/L) was below the NaCl solubility limit. Thus, high water recovery levels are possible for NID devices using 70 mM influent.

### Conclusions

A new device concept, referred to as Na-Ion Desalination (NID), has been introduced to desalinate NaCl from water by using symmetric Na-ion intercalation-electrodes separated by Na-blocking membranes. Simulated results from a two-dimensional, flowing porous-electrode model show that the type of Na-ion intercalant used affects energy consumption. The simulation shows that the proposed cell can efficiently desalinate seawater levels of NaCl at a water recovery of 50% with 0.74 kWh/m<sup>3</sup> desalination energy. Comparison of performance between cells with a Na-ion battery-separator and an anion-selective membrane indicates that selectivity is essential to achieve substantial degrees-of-desalination. Better Na-ion electroactive materials may be available,<sup>24</sup> as well as improvements to the NMO material itself using nanowires<sup>33</sup> or sub-micron slabs<sup>34</sup> that double its capacity. Further, current-density and electrode-thickness ranges are identified that minimize energy consumption and maximize desalinated water throughput. Water-recovery levels as high as 80% are achievable with 700 mM influent (where it is limited by NaCl solubility), while water-recovery levels up to 95% were predicted for 70 mM influent.

We note that the present simulations do not account for many real-world factors like electroactive-material stability in aqueous media, side reactions, solid/electrolyte interphase formation, competing cation intercalation effects (between Na<sup>+</sup>, K<sup>+</sup>, Mg<sup>2+</sup> and Ca<sup>2+</sup> in seawater), fouling/scaling in microporous electrodes, and pumping solution through microporous electrodes. In light of these non-ideal effects, the present findings should be interpreted as optimistic predictions for the performance of NID cells, and these effects must be considered during experimental demonstration that we plan to perform. Future development of the present device will benefit from on-going research in Na-ion batteries. We also note that little-to-no porous-electrode models of Na-ion and aqueous batteries have been attempted to date (to our knowledge), and the fidelity of the present model can be enhanced in the future.

### Acknowledgments

KCS and RD thank the Department of Mechanical Science and Engineering at the University of Illinois at Urbana-Champaign for financial support.

### List of Symbols

$a$	volumetric surface-area, m <sup>2</sup> /m <sup>3</sup>
$c_e$	salt concentration, mol/m <sup>3</sup>
$c_{s,max}$	solid-phase concentration of Na at saturation, mol/m <sup>3</sup>
$D_0$	bulk salt diffusivity, m <sup>2</sup> /s
$D_{eff}$	effective salt diffusivity, m <sup>2</sup> /s
$E_d$	desalination energy, kWh/m <sup>3</sup>
$F$	Faraday's constant, C/mol
$i_0$	exchange current-density, A/m <sup>2</sup>
$i_n$	local reaction current-density, A/m <sup>2</sup>
$k$	kinetic rate-constant, mol/m <sup>2</sup> -s per (mol/m <sup>3</sup> ) <sup>1.5</sup>
$R_g$	universal gas constant, J/mol-K
$s$	degree of desalination, -
$s_+$	cation stoichiometry for a salt molecule, -
$t$	time, s

$t_+$	transference number of Na ion, -
$T$	temperature, K
$u_s$	superficial velocity of electrolyte, m/s
$\vec{v}_s$	superficial-velocity vector of electrolyte, m/s
$w$	electrode thickness, m
$x$	coordinate along flow direction, m
$x_{Na}$	intercalated-Na fraction, -
$y$	coordinate along electrode thickness, m

### Greek

$\epsilon$	porosity, -
$\eta$	overpotential, V
$\kappa_0$	bulk ionic-conductivity, S/m
$\kappa_{eff}$	effective ionic-conductivity, S/m
$v_s$	volume fraction of electroactive material, -
$\sigma_s$	effective electronic-conductivity, S/m
$\Delta\Phi$	time-averaged polarization, V
$\phi_e$	solution-phase potential, V
$\phi_{eq}$	equilibrium potential, V
$\phi_{ES}$	electrostatic potential, V
$\phi_s$	solid-phase potential, V
$\chi$	electroactive-material utilization, -

### References

- Q. Schiermeier, *Nature*, **505**, 10 (2013).
- N. Ghaffour, T. M. Missimer, and G. L. Amy, *Desalination*, **309**, 197 (2013).
- M. Elimelech and W. A. Phillip, *Science*, **333**, 712 (2011).
- F. A. AlMarzooqi, A. A. Al Ghaferi, I. Saadat, and N. Hilal, *Desalination*, **342**, 3 (2014).
- John W. Blair and George W. Murphy, in *Saline Water Conversion, Advances in Chemistry*, vol. 27, p. 206, American Chemical Society (1960).
- S. Porada, R. Zhao, A. van der Wal, V. Presser, and P. M. Biesheuvel, *Prog. Mater. Sci.*, **58**, 1388 (2013).
- P. M. Biesheuvel and A. van der Wal, *J. Membr. Sci.*, **346**, 256 (2010).
- H. Li and L. Zou, *Desalination*, **275**, 62 (2011).
- M. E. Suss et al., *Energy Environ. Sci.*, **5**, 9511 (2012).
- J. Lee, S. Kim, C. Kim, and J. Yoon, *Energy Environ. Sci.*, **7**, 3683 (2014).
- H. Strathmann, *Desalination*, **264**, 268 (2010).
- W. E. Katz, *Desalination*, **28**, 31 (1979).
- K. Dermentzis, *Electrochimica Acta*, **53**, 2953 (2008).
- K. Dermentzis and K. Ouzounis, *Electrochimica Acta*, **53**, 7123 (2008).
- M. Sadrzadeh and T. Mohammadi, *Desalination*, **221**, 440 (2008).
- H. Jeon, H. Lee, K. H. Kang, and G. Lim, *Sci. Rep.*, **3**, 3483 (2013) <http://www.nature.com/srep/2013/131219/srep03483/full/srep03483.html>.
- K. N. Knust, D. Hlushkou, R. K. Anand, U. Tallarek, and R. M. Crooks, *Angew. Chem. Int. Ed.*, **52**, 8107 (2013).
- T. F. Fuller, M. Doyle, and J. Newman, *J. Electrochem. Soc.*, **141**, 1 (1994).
- C. Delmas, F. Cherkaoui, A. Nadiri, and P. Hagenmuller, *Mater. Res. Bull.*, **22**, 631 (1987).
- S. I. Park, I. Gocheva, S. Okada, and J. Yamaki, *J. Electrochem. Soc.*, **158**, A1067 (2011).
- F. Sauvage, L. Laffont, J.-M. Tarascon, and E. Baudrin, *Inorg. Chem.*, **46**, 3289 (2007).
- J. F. Whitacre, A. Tevar, and S. Sharma, *Electrochem. Commun.*, **12**, 463 (2010).
- X. Wu et al., *ChemSusChem*, **7**, 407 (2014).
- S. Hartung et al., *ChemPhysChem*, **15**, 2121 (2014).
- V. L. Chevrier and G. Ceder, *J. Electrochem. Soc.*, **158**, A1011 (2011).
- S. P. Ong et al., *Energy Environ. Sci.*, **4**, 3680 (2011).
- V. Palomares, M. Casas-Cabanas, E. Castillo-Martínez, M. H. Han, and T. Rojo, *Energy Environ. Sci.*, **6**, 2312 (2013).
- A. D. Tevar and J. F. Whitacre, *J. Electrochem. Soc.*, **157**, A870 (2010).
- X. Zhou, R. K. Guduru, and P. Mohanty, *J. Mater. Chem. A*, **1**, 2757 (2013).
- W. Wu, A. Mohamed, and J. F. Whitacre, *J. Electrochem. Soc.*, **160**, A497 (2013).
- H. Güler and F. Kurtuluş, *Mater. Chem. Phys.*, **99**, 394 (2006).
- Z. Li, D. B. Ravnsbæk, K. Xiang, and Y.-M. Chiang, *Electrochem. Commun.*, **44**, 12 (2014).
- Y. Cao et al., *Adv. Mater.*, **23**, 3155 (2011).
- M. Xu et al., *RSC Adv.*, **4**, 38140 (2014).
- M. Pasta, C. D. Wessells, Y. Cui, and F. La Mantia, *Nano Lett.*, **12**, 839 (2012).
- R. Tamamushi, *Bull. Chem. Soc. Jpn. - Bull Chem Soc Jpn.*, **46**, 2701 (1973).
- J. Newman and K. E. Thomas-Alyea, *Electrochemical Systems*, p. 672, John Wiley & Sons, (2012).
- Z. Li, D. Young, K. Xiang, W. C. Carter, and Y.-M. Chiang, *Adv. Energy Mater.*, **3**, 290 (2013).
- M. Doyle, J. Newman, A. S. Gozdz, C. N. Schmutz, and J.-M. Tarascon, *J. Electrochem. Soc.*, **143**, 1890 (1996).

40. K. E. Thomas, J. Newman, and R. M. Darling, in *Advances in Lithium-Ion Batteries*, W. A. van Schalkwijk and B. Scrosati, Editors, p. 345, Springer, US (2002).
41. D. J. Kim et al., *J. Power Sources*, **244**, 758 (2013).
42. V. R. Subramanian, V. D. Diwakar, and D. Tapriyal, *J. Electrochem. Soc.*, **152**, A2002 (2005).
43. M. Della Monica, G. Petrella, A. Sacco, and S. Büfo, *Electrochimica Acta*, **24**, 1013 (1979).
44. T. K. Perkins and O. C. Johnston, *Soc. Pet. Eng. J.*, **3**, 70 (1963).
45. J. F. Chambers, J. M. Stokes, and R. H. Stokes, *J. Phys. Chem.*, **60**, 985 (1956).
46. W. Lai and F. Ciucci, *Electrochimica Acta*, **56**, 4369 (2011).
47. P. M. Biesheuvel, R. Zhao, S. Porada, and A. van der Wal, *J. Colloid Interface Sci.*, **360**, 239 (2011).
48. R. White, C. Walton, H. Burney, and R. Beaver, *J. Electrochem. Soc.*, **133**, 485 (1986).
49. G. Liu et al., *J. Electrochem. Soc.*, **154**, A1129 (2007).
50. K. C. Smith, Y.-M. Chiang, and W. C. Carter, *J. Electrochem. Soc.*, **161**, A486 (2014).
51. V. P. Nemani, S. J. Harris, and K. C. Smith, *J. Electrochem. Soc.*, **162**, A1415 (2015).
52. Yvan Notay, *AGMG Software and Documentation*, <http://homepages.ulb.ac.be/~ynotay/AGMG>(2015).
53. Yvan Notay, *Electron. Trans. Numer. Anal.*, **37**, 123 (2010).
54. Y. Notay, *SIAM J. Sci. Comput.*, **34**, A2288 (2012).
55. A. Napov and Y. Notay, *SIAM J. Sci. Comput.*, **34**, A1079 (2012).
56. P. Albertus and J. Newman, *Dualfoil 5 Program and Documentation* <http://www.cchem.berkeley.edu/jsngrp/fortran.html> (2015).
57. M. Doyle, T. F. Fuller, and J. Newman, *J. Electrochem. Soc.*, **140**, 1526 (1993).
58. T. D. Clayton and R. H. Byrne, *Deep Sea Res. Part Oceanogr. Res. Pap.*, **40**, 2115 (1993).
59. P. M. Biesheuvel, *J. Colloid Interface Sci.*, **332**, 258 (2009).



## Comment on: “Na-Ion Desalination (NID) Enabled by Na-Blocking Membranes and Symmetric Na-Intercalation: Porous-Electrode Modeling” [*J. Electrochem. Soc.*, 163, A530 (2016)]

Kyle C. Smith\*<sup>z</sup> and Rylan Dmello

Department of Mechanical Science and Engineering and Computational Science and Engineering Program,  
University of Illinois at Urbana-Champaign, Urbana, Illinois 61801, USA

The relationship between pore-scale velocity and superficial velocity was incorrectly described in the original manuscript [*Journal of the Electrochemical Society*, 163(3) A530–A539 (2016)] and has been corrected here. Two equations in the original manuscript that expressed the superficial velocity contained erroneous factors that have been removed, as well. Further, the equation for membrane polarization presented originally contained a sign error that has been corrected here. In all cases, the results originally presented utilized the correct equations, and therefore no results were affected by these errors. In addition, several technical terms have been updated and their meanings clarified here.

© 2016 The Electrochemical Society. [DOI: 10.1149/2.0601610jes] All rights reserved.

Manuscript received August 3, 2016. Published August 13, 2016.

In the original paper a uniform, one-dimensional superficial velocity  $u_s$  was used to model the flow of electrolyte through porous electrodes. Pore-scale mean velocities were also reported for several different current and flow conditions. The values presented for each of these parameters were correct, but the relationship between the pore-scale mean velocity and the superficial velocity was stated incorrectly as “the product of porosity and superficial velocity.” Pore-scale mean velocity is equal to superficial velocity divided by porosity, not multiplied by it.

Numerical predictions for several limiting cases were compared to analytical models for validation. The analytical expression predicted by Faraday’s Law for the average effluent concentration  $\bar{c}_e^{out}$  of a membrane-based cell with superficial velocity  $u_s$  contained an erroneous factor of electrode porosity  $\varepsilon$  shown. The correct expression takes the following form:  $\bar{c}_e^{out} = c_e^{in} \pm iL/wFu_s$ , where  $c_e^{in}$ ,  $i$ ,  $L$ ,  $w$ , and  $F$  are the inlet concentration, space-averaged applied current-density, current-collector length, electrode thickness, and Faraday’s constant, respectively. Numerical predictions were compared with the correct expression for average effluent concentration, and, thus, no corrections of the results presented are required.

The energy consumed per unit volume of desalinated water  $E_d$  was defined with an erroneous factor of electrode porosity  $\varepsilon$  shown. The correct expression takes the following form:  $E_d = L \int V_{cell} i dt / u_{s,d} w \Delta t$ , where  $L$ ,  $V_{cell}$ ,  $i$ ,  $u_{s,d}$ ,  $w$ , and  $\Delta t$  are the current-collector length, cell voltage at time  $t$ , space-averaged applied current density, superficial velocity in the desalinating electrode, electrode thickness, and the total elapsed time for the desalination process, respectively. The correct expression was used to obtain all values of energy consumption presented in the original paper, and, thus, this error has no impact on the original results.

The equations for the membrane potential of an anion-exchange membrane were written with two sign errors in the original paper (p. A532). We emphasize here that the electrostatic potential  $\phi_{ES}$  and the solution-phase potential  $\phi_e$  are different quantities. The electrostatic potential  $\phi_{ES}$  is defined as the reduced electric potential in the solution, while the solution-phase potential  $\phi_e$  is defined as the reduced electrochemical potential of  $\text{Na}^+$  in solution.<sup>1</sup> The corrected electrostatic potential drop across a membrane with ideal anion permselectivity is expressed for NaCl electrolyte with unit activity coefficients as (Ref. 2, p. 375),

$$\phi_{ES,+} - \phi_{ES,-} = \frac{R_g T}{F} \ln \left( \frac{c_{e,+}}{c_{e,-}} \right) = -\frac{R_g T}{F} \ln \left( \frac{c_{e,-}}{c_{e,+}} \right). \quad [1]$$

We note that the membrane-potential model presented in the reference originally cited<sup>3</sup> reproduces this potential drop in the limit of high ion-exchanger capacity. As described in our original paper, membrane polarization can also be addressed in terms of the solution-phase potential  $\phi_e$  according to its definition as the reduced electrochemical potential of  $\text{Na}^+$ ,<sup>1</sup>

$$\phi_e = \phi_{ES} + \frac{R_g T}{F} \ln(c_e). \quad [2]$$

Solving Eq. 2 for  $\phi_{ES}$  and substituting into Eq. 1 we find the correct expression for solution-phase potential drop across the membrane,

$$\phi_{e,+} - \phi_{e,-} = \frac{2R_g T}{F} \ln \left( \frac{c_{e,+}}{c_{e,-}} \right) = -\frac{2R_g T}{F} \ln \left( \frac{c_{e,-}}{c_{e,+}} \right). \quad [3]$$

The correct expressions were implemented in the original model, and, thus, these corrections do not impact the original results.

Throughout the paper, the term “intercalant” was used inaccurately to describe intercalation host compounds, when in fact “intercalant” refers to the species undergoing intercalation (which was  $\text{Na}^+$  in the modeled device). In addition, the terms “cathode” and “anode” were used, respectively, to refer to the positive and negative terminals across which cell voltage was measured. This is conventional nomenclature used in the rechargeable Li-ion and Na-ion battery communities, but, strictly speaking, these designations are consistent with the definitions of cathodic and anodic processes only during cell discharging (i.e., when current flows from the negative to the positive electrode) and not during cell charging. Finally, in several instances the terms “charge cycle,” “discharge cycle,” and “charging cycle” were used to describe either a charge or discharge step in a complete charge/discharge cycle. In these respective instances the correct terminology is “charge process,” “discharge process,” and “charging process.”

### References

1. W. Lai and F. Ciucci, “Mathematical modeling of porous battery electrodes—Revisit of Newman’s model,” *Electrochimica Acta*, **56**, 4369 (2011).
2. F. G. Helfferich, *Ion Exchange*. Courier Corporation; 1962.
3. P. M. Biesheuvel, R. Zhao, S. Porada, and A. van der Wal, “Theory of membrane capacitive deionization including the effect of the electrode pore space,” *J Colloid Interface Sci.*, **360**, 239 (2011).

\*Electrochemical Society Member.

<sup>z</sup>E-mail: kcsmith@illinois.edu